Unravelling the interfacial dynamics of band-gap funneling in bismuth-based halide perovskites

Yunqi Tang[a,b,†], Chun Hong Mak[a,b,†], Jun Zhang[c], Guohua Jia[d], Kuan-Chen Cheng, Haisheng Song[e], Mingjian Yuan[f], Shijun Zhao[,c], Ji-Jung Kai[c], Juan Carlos Colmenares[g], and Hsien-Yi Hsu[*,a,b]*

Dr. Y. Tang, C. Hong Mak and Prof. H.-Y. Hsu

School of Energy and Environment & Department of Materials Science and Engineering, City University of Hong Kong, Kowloon Tong, Hong Kong, China.
E-mail: sam.hyhsu@cityu.edu.hk

Dr. Y. Tang, C. Hong Mak and Prof. H.-Y. Hsu

Shenzhen Research Institute of City University of Hong Kong

Shenzhen 518057, P. R. China

J. Zhang, Prof. S. Zhao and Prof. J.-J. Kai

Department of Mechanical Engineering, City University of Hong Kong, Kowloon Tong, Hong Kong, China.

Prof. G. Jia
Curtin Institute of Functional Molecules and Interfaces

School of Molecular and Life Sciences

Curtin University

GPO Box U1987, Perth, WA 6845, Australia

This is the author manuscript accepted for publication and has undergone full peer review but has not been through the copyediting, typesetting, pagination and proofreading process, which may lead to differences between this version and the Version of Record. Please cite this article as doi: 10.1002/adma.202207835.

Prof. H. Song

Wuhan National Laboratory for Optoelectronics (WNLO) and School of Optical and Electronic Information, Huazhong University of Science and Technology, 1037 Luoyu Road, 430074, Wuhan, Hubei, P. R. China

Prof. J. C. Colmenare

Institute of Physical Chemistry, Polish Academy of Sciences, 01-224 Warsaw, Poland

Keywords: interfacial dynamics, lead-free halide perovskite, photoelectrocatalysis

Corresponding author: shijzhao@cityu.edu.hk and sam.hyhsu@cityu.edu.hk

Y. Tang and C. H. Mak contributed equally to this work.

We have developed an environmentally friendly mixed-halide perovskite $MA_3Bi_2Cl_{9-x}I_x$ with a band-gap funnel structure. However, the dynamic interfacial interactions of band-gap funneling in $MA_3Bi_2Cl_{9-x}I_x$ perovskites in the photoelectrochemical (PEC) system remain ambiguous. In light of this, we prepared single- and mixed-halide lead-free bismuth-based hybrid perovskites—$MA_3Bi_2Cl_{9-y}I_y$ and $MA_3Bi_2I_9$ (named MBCl-I and MBI)—in the presence and absence of the band-gap funnel structure, respectively. Using temperature-dependent transient photoluminescence and electrochemical voltammetric techniques, we therefore confirmed the photophysical and (photo)electrochemical phenomena of solid–solid and solid–liquid interfaces for MBCl-I and MBI halide perovskites. Concerning the mixed-halide hybrid perovskites MBCl-I with a band-gap funnel structure, stronger electronic coupling arising from an enhanced overlap of electronic wavefunctions results in more efficient exciton transport. Besides, MBCl-I's effective diffusion coefficient and electron transfer rate demonstrate efficient heterogeneous charge transfer at the solid–liquid interface, generating improved photoelectrochemical hydrogen production. Consequently, this combination of photophysical and electrochemical techniques opens up an avenue to explore the intrinsic and interfacial properties of semiconductor materials for elucidating the correlation between material characterisation and device performance.

1. Introduction

The light-driven conversion of solar energy into hydrogen energy or other value-added chemicals represents a promising technique to overcome energy shortage and environmental issues.[1] The photoelectrochemicals (PEC) technique, which elaborately integrates a light harvester and an electrochemical catalyst into an independent system, has been recognised as an effective approach in producing hydrogen fuels.[2] However, most representative metal oxide photoelectrodes have unfavourable PEC properties—limited light-harvesting capability, high exciton recombination rates, complex manufacturing process, and poor solar-to-product efficiency[3]—that may restrict their practicable applications. In the past few years, halide perovskite materials with the typical structures of ABX_3 or $A_3B_2X_9$ have been broadly applied in solar energy conversion because of their intrinsic properties—broad solar absorption, long exciton diffusion length, high charge-carrier mobility, facile fabrication process, and effective energy-conversion efficiency—that are advantageous to PEC hydrogen (H_2) production.[4] Though progress has been made by using Pb-based hybrid perovskites for solar-to-energy conversion, halide perovskites are highly sensitive to moisture, which leads to their degradation in water—a deficiency considerably challenges H_2 evolution with halide perovskite photocatalysts in an aqueous solution.

To tackle this stability problem, methylammonium lead iodide ($MAPbI_3$) photocatalysts with a Pt co-catalyst have been adopted in dynamic equilibrium with a saturated hydrogen iodide (HI) aqueous solution for HI splitting.[5] Subsequently, Wu et al.[6] prepared a $MAPbI_3$ perovskite coupled with reduced graphene oxide for visible-light-driven H_2 evolution in an aqueous HI solution. To improve the performance of the aforementioned systems, halide perovskite photocatalysts—$MAPbBr_{3-x}I_x$ and $FAPbBr_3$—were prepared.[6-7] Although Pb-based halide perovskites with improved

conversion efficiency have been reported, the toxicity of Pb to human life, due to their high solubility in water, limits their potential for widespread applications. On the other hand, bismuth (Bi)-based perovskites have been confirmed to provide a non-toxic and chemically stable alternative for solar-fuel applications.[8] Among them, methylammonium bismuth iodide ($MA_3Bi_2I_9$ or MBI) possesses a hexagonal structure, with isolated $Bi_2I_9^{3-}$ ions forming the face-sharing Bi–I octahedra.[9] Besides, it has been proved that Bi-based perovskites possess satisfactory stability and that their photoluminescence quantum yield is less than that of their Pb-based analogues—in other words, Bi-based perovskites with low charge-carrier recombination benefits hydrogen production performance.[10]

Despite the innovation of halide perovskite photocatalysts for H_2 generation, their photocatalytic efficiency must be further improved to meet basic requirements for practical applications. Instead of using the photocatalytic system, Luo et al.[11] performed a PEC H_2 evolution using the $MAPbI_3/TiO_2$ photoelectrode, in which the amount of H_2 evolution was found to be considerably increased due to the enhanced charge separation rate induced by the external bias potential. We were thus motivated to design an efficient and stable photo-electrocatalyst. Recently, we successfully developed a mixed-halide perovskite MBCl-I (i.e., $MA_3Bi_2Cl_{9-y}I_y$), in which the distribution of I^- in MBCl-I gradually decreased from the surface to the interior, forming a band-gap funnel structure.[12] However, the dynamic interactions of the halide perovskite itself and at the interface between the photoelectrode and the electrolyte remain unknown. In light of this, we designed MBCl-I and MBI (i.e., $MA_3Bi_2I_9$) halide perovskites with and without the band-gap funnel structure, respectively, to study the exciton transport and electrochemical dynamics of band-gap funneling in halide perovskites between the interfaces. Using a combination of photophysical and

electrochemical techniques, we report the fundamental properties (e.g., exciton transfer dynamics, electrochemical redox activity, and charge transfer features). Regarding the electron-hole pair diffusion of MBI and MBCl-I perovskites by temperature-dependent transient photoluminescence (TRPL), MBCl-I's electronic coupling was found to show a substantial increase compared to its MBI counterpart. In addition, we used cyclic voltammetry (CV) at various scan rates and found that MBCl-I's diffusion coefficient and electron transfer rate constant with the band-gap funnel structure at the electrode/electrolyte interface is substantially enhanced, therefore leading to high-performance PEC hydrogen generation as a result of efficient heterogeneous charge transfer.

2. Results and discussions

2.1. Material design and DFT calculation

To determine the interfacial photophysical dynamics and electrochemical kinetics of the solid–solid and solid–liquid interfaces for band-gap funneling in halide perovskites, we synthesised the MBCl-I and MBI halide perovskites based on our recent publication.[12] For the iodide/chloride-mixed MBCl-I, we have confirmed that the iodide element concentration decreases from the surface to the interior across the MBCl-I perovskite.[12] To fabricate the MBCl-I (or MBI)/FTO photoelectrodes, the as-synthesised MBCl-I (or MBI) powders were dissolved into ethanol and continuously stirred until the uniform distribution was achieved. The MBCl-I (or MBI) solution was then deposited onto the FTO by drop-casting. Specifically, scotch tape was used to control the thickness of the semiconductor films on the FTO substrate. Finally, to complete the fabrication of the MBCl-I (or MBI) /FTO photoelectrodes for PEC hydrogen evolution, the MBCl-I (or MBI)/FTO samples were transferred to a hot plate at 90^{o}C for 1h.

As **Figure 1**a shows, the XRD pattern of the MBCl-I powder samples is similar to that of MBI, indicating no obvious difference between the frames of MBCl-I and MBI. However, there exists an approximately 0.2-degree shift of MBCl-I in the XRD pattern compared with MBI, illustrating that, when HI is added to the reaction system, chloride ions are replaced by iodide elements without any changes to the perovskite crystal structure. Figure S1, Supporting Information, shows the XRD patterns of the MBCl-I and MBI thin films. Apparently, there is no evident difference between the powder samples and thin films—the ethanol and heat treatment did not change the structure of MBCl-I and MBI. The SEM images, as shown in **Figure 1**b and **1**c, confirm that the MBCl-I and MBI perovskite films deposited on the FTO glass are compact and uniform. Moreover, as the high-magnification SEM images (Figure S2, Supporting Information) reveal, the MBCl-I and MBI perovskite films exhibit a morphology similar to that of their perovskite powder samples, which indicates that ethanol and heat treatment do not change the perovskite structure. In **Figure 1**d, the crystal structure of the MBI is hexagonal with the space group of P63/*mmc*, which is consistent with the previous report.[13] Moreover, the unit cell of MBI (i.e., $MA_3Bi_2I_9$) consists of two isolated face-sharing $Bi_2I_9^{3-}$ octahedra surrounded by methylammonium cations.

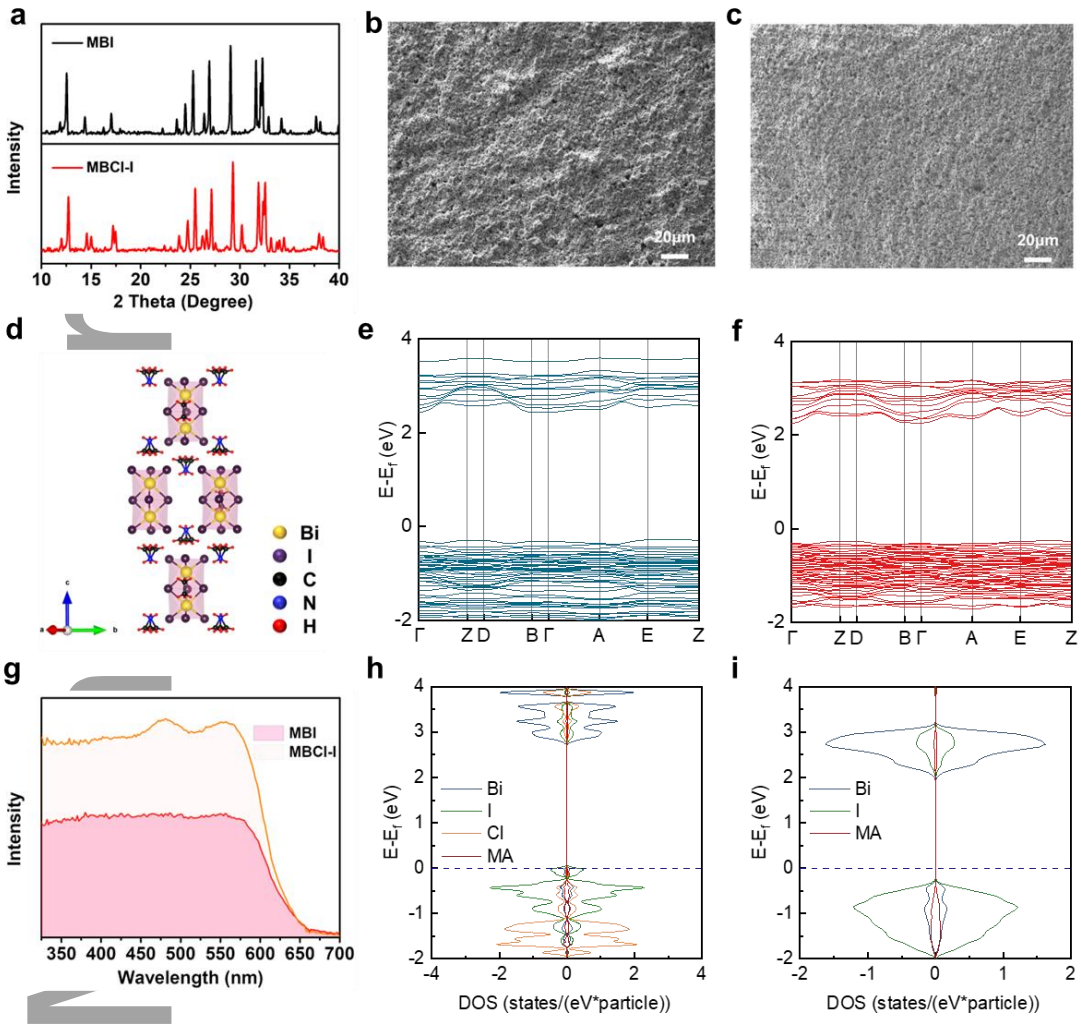

Figure 1. a) Powder X-ray diffraction (XRD) patterns of MBI and MBCl-I. SEM image of b) MBCl-I and c) MBI photoelectrodes. d) Crystal-structural model of the MBI. Band structure of e) MBCl-I and f) MBI. g) UV-vis diffuse reflectance spectra of MBCl-I and MBI. Density of states (DOS) of h) MBCl-I and i) MBI.

For density functional theory (DFT) calculations, the crystal structure characterised by Eckhardt et al.[14] was adopted to model the MBCl-I and MBI systems. The bulk structure was optimised with self-consistent calculations by expanding and compressing the crystal (Figure S 3, Supporting

Information), and the calculated lattice constants are listed in Table S1, Supporting Information. Based on the band structures (**Figure 1**e and **1**f) and the density of states (DOS) (**Figure 1**h and **1**i), the band-gap of iodide/chloride-mixed MBCl-I is larger than MBI single-halides perovskites. Accordingly, these results disclose the presence of a band-gap funnel structure in MBCl-I perovskites, a finding consistent with previous reports.[12] Additionally, the projected DOS shows that the valence and conduction bands are dominated by I and Bi bands in both MBCl-I and MBI systems (**Figure 1**h and **1**i).

Moreover, to quantify the effect of mixed-halide perovskites, MBCl-I, in the charge distribution, Bader charge calculations were performed. As indicated in Table S2, Supporting Information, Cl atoms attract more electrons than I from the connecting Bi atoms. In comparison, the introduction of Cl was found to have little impact on the charge of the C, N, and H elements. Further, the partial charge density of the valence band maximum (VBM) and conduction band minimum (CBM) was calculated. As Figure S5, Supporting Information, shows, the VBM and CBM are mainly occupied by electrons from I and Bi, respectively. The Cl atoms show a lower charge density than I near the Fermi level, agreeing well with the DOS analysis.

To investigate the optical properties of MBCl-I and MBI, ultraviolet-visible (UV-vis) diffuse reflectance spectroscopy and steady-state photoluminescence (PL) spectra were conducted (**Figure 1**g and Figure S6, Supporting Information). Between the 400 and 800 nm wavelength region, the FTO-coated glass was found to have no absorption.[15] After coating the perovskite on FTO, an evident absorption in the range from 350 nm to 650 nm was observed, indicating that this bismuth-based perovskite can be an efficient visible-light harvester. In addition, there is a steep absorption edge at about 650 nm, which matches well with the reported literature.[16] To gain more information

about the factors that can affect the PEC performance of MBCl-I/FTO and MBI/FTO photoelectrode, steady-state photoluminescence (PL) measurements were performed. The PL spectra of the halide perovskites present a single emission peak centred at about 625 nm (Figure S6, Supporting Information), which is consistent with the reported publication.[17] Noticeably, we compared the PL spectra of the MBCl-I/FTO and MBI/FTO photoelectrodes, and the MBCl-I/FTO displayed a lower PL intensity, suggesting the lower recombination of photogenerated electron-hole pairs, which benefits the PEC performance.

To evaluate the emission properties of the as-prepared MBCl-I and MBI, PL decays under an excitation wavelength of 450 nm were monitored at 625 nm using a transient photoluminescence (TRPL) spectrometer. **Figures 2**a and **2**c show the PL decay curves modelled by a bi-exponential function containing a short-lived (τ_1) and a long-lived lifetime (τ_2) component. The short component (τ_1) is ascribed to non-radiative recombination related to interface defect, and the long component (τ_2) is attributed to radiative recombination related to bulk properties.[18] The PL intensity of MBCl-I mixed-halide perovskites at room temperature (20°C) is dominated by the fast decay component with the time constant of τ_1 (9.1 ns), followed by a slower decay (τ_2 = 307 ns), as listed in Table S3 and S4, Supporting Information. The MBCl-I/FTO photoelectrode shows an average lifetime (τ_{ave}) of ~ 45.2 ns at room temperature. The PL lifetime of the MBI single-halide perovskites is 17.1 ns, which is faster than that of the MBCl-I analogues, indicating that the band-gap funneling in bismuth-based halide perovskite MBCl-I can prolong the lifetime of the photo-induced charge carriers. This phenomenon aligns with the PL result and previous literature.[19]

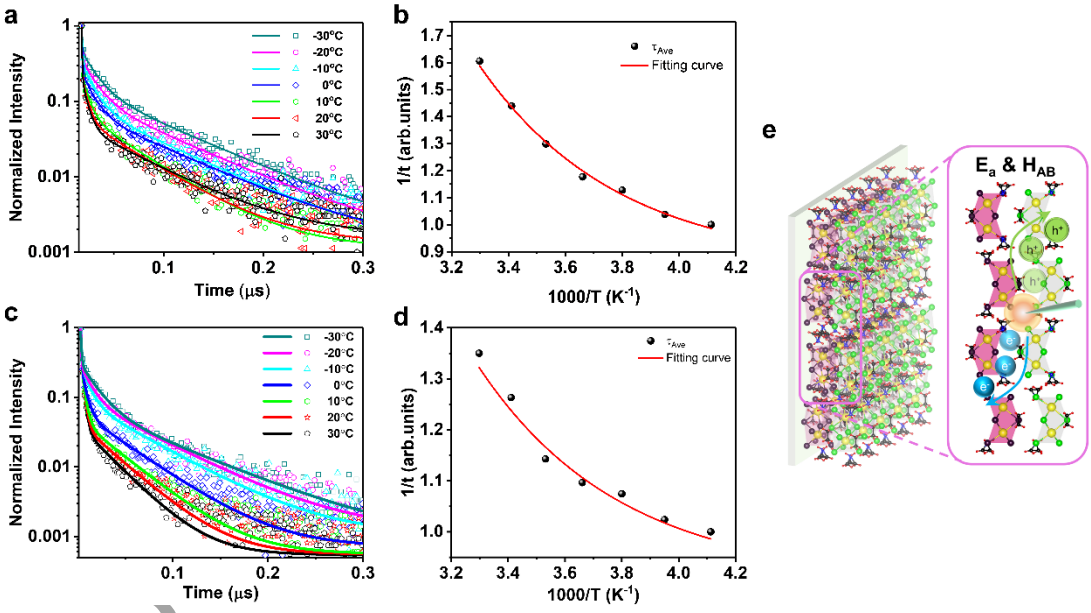

Figure 2. Temperature-dependent TRPL decay curves of a) MBCl-I and c) MBI. Arrhenius plots of b) MBCl-I and d) MBI. The red curves correspond to equation $1/\tau = a \times \sqrt{1/T} exp[-E_a/k_B T] + b$. e) Schematic diagram of the exciton transport of photogenerated electron-hole pairs.

2.2. Temperature-dependent exciton dynamics

The efficient electron-hole separation and electron transport of photogenerated electron-hole pairs can theoretically result in enhanced PEC hydrogen production. It has been proved that the temperature-dependent TRPL can be adopted to explain the transportation of electron-hole pairs.[20] To investigate the influence factor of the motion of electron-hole pairs of the participate perovskites, temperature-dependent TRPL was conducted under an excitation wavelength at 450 nm with temperature ranging from – 30 ℃ to 30 ℃. As shown in **Figure 2**a and **2**c, the lifetime of the participated bismuth-based perovskites was found to decrease with an increase in temperature.

The energy and electron transfer mechanisms of electron-hole pairs have been explained by Förster theory, Dexter theory, and Marcus theory.[20d, 20e, 21] According to the Förster resonance energy transfer (FRET) theory, the energy migration is driven by the resonant coupling of the electrical dipoles between an excited donor and an acceptor. Dexter's theory supposes that the energy transfer is the exchange of electrons in the highest occupied molecular orbital (HOMO) and the lowest unoccupied molecular orbital (LUMO) between the donor and the acceptor molecules.[20a] Marcus theory has also been broadly used to explain the electron transfer in distinct molecular systems.[18d, 22] Some previous reports have proved that the Marcus theory can also be adopted to explain the transfer of electron-hole pairs.[20a, 23]

Here, we apply the Marcus theory to illustrate the electron-hole pair's behaviour of the participated samples in the PEC reaction process. Generally, the classical Marcus theory[22a, 24] can be used to express the rate constant of electron transfer, k_{et}, as shown in Equation (1):

$$k_{et} = \frac{2\pi}{\hbar}|H_{AB}|^2\sqrt{\frac{1}{4\pi k_B T\lambda}}\exp\left[-\frac{E_a}{k_B T}\right] \quad (1)$$

where $|H_{AB}|$ is the electronic coupling between the initial state *A* and the final state *B*;; $\hbar$ is the reduced Planck's constant; k_B is the Boltzmann constant; T is the temperature (K); and E_a is the activation energy.

Furthermore,

$$\frac{1}{\tau} = k = k_{et} + b \quad (2)$$

where τ is the recombination lifetime (i.e., $\tau_1$and τ_2) of the slow and fast decay components of the measured sample; k is the exponential decay constant or rate constant, and the constant b represents the sum of the temperature-independent non-radiative and radiative decay rates.

$$\frac{1}{\tau} = k_{et} + b = \frac{2\pi}{\hbar}|H_{AB}|^2\sqrt{\frac{1}{4\pi k_B T\lambda}}\exp\left[-\frac{E_a}{k_B T}\right] + b \quad (3)$$

A simplified equation is then expressed as follows:

$$1/\tau = a \times \sqrt{1/T}exp[-E_a/k_B T] + b \quad (4)$$

with a= $\frac{2\pi}{\hbar}|H_{AB}|^2\sqrt{\frac{1}{4\pi k_B\lambda}}$

When the donor molecules are identical to the acceptor ones, the electron transfer reaction is in an isoenergetic situation. The activation energy is thus dependent only on the reorganisation energy λ for the equilibrium thermodynamic free energy of the donor and acceptor:

$$E_a = \frac{\lambda}{4} \quad (5)$$

On the basis of the temperature-dependent TRPL spectral response of the MBCl-I (**Figure 2**a), the activation energies of the fast and slow decay components are about 198 meV and 167 meV, which were obtained by fitting the PL decay curves using the equation $1/\tau = a \times \sqrt{1/T}exp[-E_a/k_B T] + b$ (**Figure 2**b, Table S3, Supporting Information and Table S5, Supporting Information). By comparison, the temperature-dependent TRPL spectra of the MBI were also collected (**Figure 2**c, **Figure 2**d, and Table S4, Supporting Information). The activation energies (i.e., 203 meV and 174 meV) for the fast and slow decay components of MBI perovskite are higher than those of MBCl-I

(198 meV and 167 meV), revealing that the electron migration of MBCl-I is much easier than that of MBI, which contributes to PEC performance. Moreover, it is known that the electronic coupling elements $|H_{AB}|$ are related to the overlap of the excited-state wave functions of the initial and final sites, which play a crucial role in the rate of the electron transfer reaction. From the pre-exponential factor of Equation (4), the temperature-independent coupling matrix elements $|H_{AB}|$ were evaluated for the fast and slow decay components of MBCl-I perovskites (0.427 cm^{-1} and 0.234 cm-1), which are stronger than those of MBI (0.339 cm-1 and 0.191 cm-1), as the wave functions of MBCl-I are more delocalised along with the perovskite materials (Table S5, Supporting Information). In contrast, such an overlap within MBI perovskites has to occur between neighbouring molecules. In Table 3 and Table S4, Supporting Information, α_1 and α_2 are the amplitudes of exciton recombination for individual photophysical processes. The fast components (α_1) of MBCl-I show large amplitudes (~ 0.86 – 0.88) at all temperatures. On the other hand, similar amplitudes α_1 (~ 0.90 – 0.91) were observed in the fast decay components of MBI, demonstrating that the non-radiative recombination resulting from the interface defects for both participated perovskite materials (i.e., MBCl-I and MBI) is the dominant photophysical process at all temperatures, which indicates that a faster decay channel is preferred for most of the excited electrons and holes of both Bi-based halide perovskites.[25] Consequently, stronger electronic coupling and lower activation energy result in enhanced exciton transfer, corroborating the finding that the mixed-halide MBCl-I with the band-gap funnel structure is a more promising PEC material than the MBI perovskite.[26]

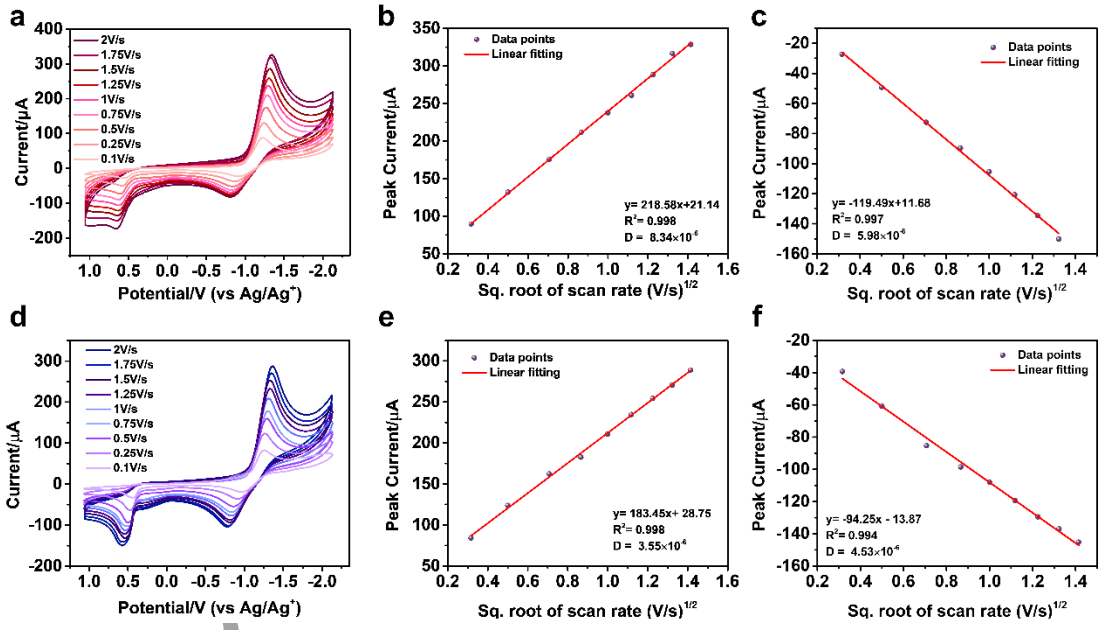

Figure 3. Cyclic voltammogram of a) MBCl-I and d) MBI in CH_2Cl_2 with 1 mM $TBAPF_6$ at various scan rates. Reduction peak current versus $v^{1/2}$ of b) MBCl-I and e) MBI. Oxidation peak current versus $v^{1/2}$ of c) MBCl-I and f MBI.

2.3. Heterogeneous electron transfer kinetics

To investigate the electrochemical characteristics of the solid–liquid interfaces between the electrode and the electrolyte—reversibility, stability, diffusion coefficient, number of electrons transferred, electron transfer efficiency—the cyclic voltammetry (CV) of MBCl-I and MBI at different scan rates from 2V/s to 0.1V/s were conducted in CH_2Cl_2 (0.1M $TBAPF_6$) electrolyte at room temperature. During the cyclic voltammetry process, the Bi-based perovskite will undergo oxidation and reduction reaction. In terms of the reduction reaction in **Figure 3**a and **3**d, the cathodic peaks of MBCl-I and MBI perovskites at − 1.22 and − 1.24 V at a scan rate of 100 mV/s shifted towards a more

negative potential as the scan rate increased and then reached − 1.34V and −1.37V at 2 V/s scan rate. Additionally, the peak-to-peak separation (ΔEp) of MBCl-I and MBI perovskites increased from 0.29 V to 0.53 V and from 0.27V to 0.55 mV with an increasing scan rate from 0.1 V/s to 2 V/s, respectively. The larger ΔEp values in the reduction reaction with increasing the scan rate demonstrate that the quasi-reversible process occurs at the electrode surface.[27] For the irreversible oxidation reaction, the anodic peaks for MBCl-I and MBI in the reverse scan appeared at − 0.52 and − 0.56V and shifted towards more positive potential with an increasing scan rate up to 2.0 V/s. The plots presented in **Figure 3**b-c and **3**e-f illustrate the linear relationship between the quasi-reversible reduction peak currents and the irreversible oxidation currents with the square root of scan rate values. All the linear regression coefficients (R^2) reached the 0.994 and 0.998 range, suggesting that the electrochemical process is a diffusion-controlled electron transfer reaction.[28] The quasi-reversibility of this electrochemical process was also verified through the linear plot of the logarithm of peak potential against the logarithm of scan rate (Figure S7, Supporting Information).[29] This logarithmic plot with the R^2 value of 0.998 shows a slope of 0.43, which is quite close to the theoretical slope (i.e., 0.5) for the diffusion-controlled reaction. Accordingly, these estimated results further prove that this oxidation–reduction reactions under our investigation is the diffusion-controlled electron-transfer process. The electrochemical characteristics of MBCl-I and MBI halide perovskites were then determined by utilising the Randles–Sevcik equation (6):

$$\mathrm{I}_{rev} = (2.69 \times 10^5) n^{3/2} A C D^{1/2} v^{1/2} \quad (6)$$

For quasi-reversible and/or irreversible systems, a general equation is given by Equation (7):[30]

$$\mathrm{I}_{irrev} = (2.99 \times 10^5) n(\alpha n')^{1/2} A C D^{1/2} v^{1/2} \quad (7)$$

In terms of equations 6 and 7, the I is peak current (A); n is the number of the exchanged electron; n' is the total number of electrons transferred before the rate-determining step; α is the transfer coefficient; A is the active surface area of the working electrode (cm^2); D is the diffusion coefficient (cm^2/s); C is the concentration (mol cm^{-3}); and v is the voltage scan rate (V/s).

The diffusion coefficient (D) of the redox (electroactive) species was then characterised with the calculated concentration (C = ~ 4 mM) using the Randles–Sevcik equation in Equation (7) to evaluate the heterogeneous electron-transfer rate constant (k^0). The Tafel plot in Figure S8, Supporting Information, was obtained from the descending parts of the cathodic and anodic peaks of the cyclic voltammogram. We then determined α using the slope of the plot of log(*i*) versus potential, as shown in Equation (8).[30b]

$$\text{Slope} = \frac{\alpha F}{2.3RT} or \frac{-\alpha F}{2.3RT} \quad (8)$$

The heterogeneous electron-transfer rate constant (k^0) was then obtained using the Gileadi method, which is based on the determination of the critical scan rate at which the reaction changes from reversible to irreversible or from quasi-reversible to irreversible.[31] The critical scan rate (V_c) was graphically evaluated by plotting E_p against the log of scan rate at low and high scan rates. Two different slopes were obtained from the two lines fitted for low and high scan rates. The intersection of the two lines provided the critical scan rate, and k^0 was determined by Equation (9).[32]

$$\log k^0 = -0.48\alpha + 0.52 + log\left(\frac{nF\alpha V_c D}{2.303RT}\right)^{\frac{1}{2}} \quad (9)$$

As listed in Table 1, the diffusion coefficients for the reduction and oxidation reactions of MBCl-I perovskites are 8.34×10^{-6} cm^2 s^{-1} and 5.98×10^{-6} cm^2 s^{-1} with high rate constants of 0.0075 cm s^{-1}

and 0.0114 cm s^{-1}, respectively. For comparison, the diffusion coefficients and rate constants of MBI halide perovskites are also listed in Table 1. Based on electrochemical characterisations and systematic discussions of electron transfer at the solid–liquid interfaces, band-gap funneling in the MBCl-I mixed-halide perovskite leads to a higher diffusion coefficient and a more rapid rate constant compared to the MBI single-halide perovskite. As a result, MBCl-I, owing to the efficient heterogeneous electron transfer in the reaction system, is definitely a promising candidate for PEC hydrogen production applications.

Table 1. The kinetic parameters of MBCl-I and MBI, including E°, D, k°, and α for MBCl-I and MBI in CH_2Cl_2/0.1 M $TBAPF_6$ at room temperature

	MBI		**MBCl-I**	
	Reduction	Oxidation	Reduction	Oxidation
E° (V)	-0.914	0.821	-0.896	0.883
10^{-6} D (cm^2 s^{-1})	3.55	4.53	8.34	5.98
α	0.13	0.64	0.24	0.33
k^o (cm s^{-1})	0.0033	0.0046	0.0075	0.0114

2.4. Electrochemical and photoelectrocatalytic characterisations

To manifest the efficient charge separation at the interface of the MBCl-I and MBI halide perovskites, electrochemical impedance spectroscopy (EIS) was conducted by applying open-circuit potential under visible-light irradiation. **Figure 4**a shows the Nyquist plots of the electrochemical impedance

of the MBCl-I and MBI systems. The arc radiuses of MBCl-I mixed-halide perovskites are smaller than that of the MBI|FTO single-halide perovskites, indicating that the MBCl-I perovskite with a band-gap funnel structure possesses a lower charge separation resistance. Thus, the charge separation and transfer process are improved between the interface of the electrode and electrolyte.[33] Notably, the space charge layer/Helmholtz layer interface can be formed by immersing a semiconductor electrode in an electrolyte. As **Figure 4**b shows, the charge-carrier (holes or electrons) transportation across the interface can be modelled using macroscopic impedance: resistors and capacitors in parallel and series.[34] The EIS Nyquist plots of the measured samples were then simulated to the equivalent electrical circuit, with the circuit elements comprising the charge transfer resistance (R1) at the electrode-electrolyte interface, the series resistance (Rs), the constant phase element (CPE), as well as the Warburg impedance (W1).[33] In the high-frequency range, the EIS spectrum can be fitted to an ideal parallel resistor and capacitor circuit. This corresponds to the space charge layer of the perovskite film.[34] At lower frequencies, the Nyquist plot shows a transition to a linear region, illustrating an additional diffusion component to the recorded overall capacitance.[34] To demonstrate this element clearly, a comparison of the fitting parameters is listed in Table S6, Supporting Information. Furthermore, Figure S9, Supporting Information, shows the Mott–Schottky (MS) plots of the MBCl-I and MBI halide perovskites taken at a frequency equal to 500 Hz. The slopes of the MS plots for MBCl-I and MBI perovskites are negative, suggesting that these perovskites are p-type charge carriers and are well-qualified for hydrogen production reaction.

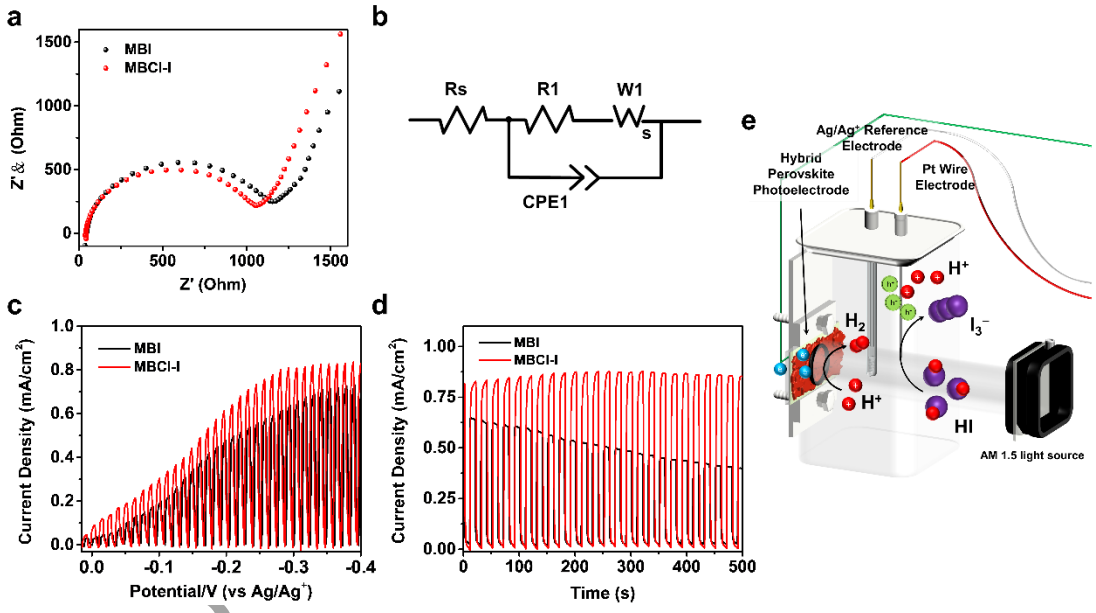

Figure 4. a) Nyquist plots of MBCl-I and MBI measured at 0.14 V versus Ag/Ag^+ electrode under visible-light irradiation in dichloromethane (CH_2Cl_2) solution containing 0.1 m tetrabutylammonium hexafluorophosphate ($TBAPF_6$) as an electrolyte solution. b) Equivalent electrical circuits of the electrochemical cell. c) Chopped photocurrent-voltage (J-V) curves recorded under visible-light illumination. d) Chopped photocurrent responses recorded at – 0.3 V vs. Ag/Ag^+ under visible-light illumination. e) Schematic illustration of the MBCl-I|FTO (or MBI|FTO) photoelectrode with the working principle of the photoelectrochemical HI splitting cell.

Figure 4c shows the chopped linear sweep voltammetry (LSV) collected from the MBCl-I|FTO and MBI|FTO perovskite-based photoelectrodes in HI solution under visible-light illumination in the three-electrode system (**Figure 4**e). Compared with the MBI|FTO films, the MBCl-I|FTO films show a pronounced photocurrent response for PEC hydrogen production in HI solution. For example, at an applied potential of − 0.3 V *vs.* Ag/Ag^+, the photocurrent density for the MBCl-I|FTO film was about

0.8 mA/cm^2, which at least increased by approximately 1.4 times that of MBI/FTO. **Figure 4**d shows the chopped photocurrent profiles of the MBCl-I|FTO and MBI|FTO photoelectrodes recorded at − 0.3 V vs. Ag/Ag$^+$. The photocurrent responses of the MBCl-I|FTO photoelectrodes are fairly repeatable in numerous illumination on-off cycles, revealing superior photostability of the photoelectrode. Additionally, the optimised MBCl-I|FTO photoelectrode can produce a photocurrent density of about 0.80 mA/cm^2 at – 0.3 V vs. Ag/Ag$^+$, which is higher than that (only 0.4 mA/cm^2) of the MBI|FTO photoelectrode after 500s of exposure. These results confirm that band-gap funneling in MBCl-I halide perovskites benefits the PEC performance of hydrogen production in HI solution. Consequently, the MBCl-I mixed-halide perovskite with the band-gap funnel structure is a relatively excellent alternative to MBI in the PEC hydrogen production reaction.

3. Conclusion

This study demonstrated an efficient bismuth-based halide perovskite-based PEC system for hydrogen production. When using temperature-dependent transient photoluminescence, MBCl-I showed increased electronic coupling and diminished activation energy than MBI. At the solid–liquid interface between the electrode and the electrolyte, the diffusion coefficient and heterogeneous electron transfer of MBCl-I were found to be more efficient than that of MBI. Consequently, the MBCl-I halide perovskites equipped with the band-gap funnel structure in the PEC device exhibited a high photocurrent density of ~ 0.80 mA cm^{-2} at − 0.3 V vs. Ag/Ag$^+$ under visible light (430 nm cutoff) illumination. As a result, the enhanced performance of MBCl-I with the band-gap funnel structure by utilising ion exchange was achieved—this offers new insights into the advancement of next-

generation PEC materials for commercial applications in the emerging field of energy-saving and energy-conversion technologies.

4. Experimental Section/Methods

Chemical and reagent.

The precursors for the synthesis of halide perovskites including methylammonium chloride (MACl, >98%) from Dickman, bismuth chloride ($BiCl_3$, >98%), and hydroiodic acid (HI) (57 wt% in water) were purchased from Energy Chemical Isopropanol (IPA, >99%) was purchased from VWR chemical. Dichloromethane (CH_2Cl_2, HPLC grade) was provided by Duksan reagents. Tetrabutylammonium hexafluorophosphate ($TBAPF_6$), were purchased from Sigma Aldrich (USA).

Synthesis of Bi halide perovskites.

The bismuth-based samples were prepared by a simple solvothermal route based on our previous work.[13] Shortly, we then added MACl and $BiCl_3$ into IPA under vigorous stirring. After the mixture became uniform, 0.2 mL HI solution was added into the above solution for an additional 30 minutes stirring. Subsequently, the mixture was transferred and sealed into a 50 mL Teflon-lined stainless-steel autoclave. The autoclave reactor was heated at 130^{o}C for 6 hours in an oven and then cooled down to room temperature. The resulting samples were collected by centrifugation and dried at 60^{o}C for 8 hours. The as-synthesized mixed-halide perovskite, $MA_3Bi_2Cl_{9-y}I_y$, is labeled as MBCl-I. The M, B, Cl, and I represent methylammonium iodide (MAI), bismuth, chlorine, and iodine, respectively. In terms of the synthesis of MBI, we used almost the same preparation procedure. For

the difference between MBCl-I and MBI, MACl and $BiCl_3$ were replaced by MAI and BiI_3 without the addition of HI to obtain single-halide perovskite $MA_3Bi_2I_9$ (label as MBI)

Preparation of perovskite-based working electrodes.

0.1mg as-prepared sample (MBCl-I or MBI) was added into 1ml ethanol and kept vigorous stirring for 30 min, and then sealed with a Teflon cap and transferred to the ultrasonic agitation overnight to make it uniform. After that, we kept vigorous stirring until the ink became a slurry.

The fluorine-doped SnO_2 (FTO) glasses were cut into 1 cm × 1.5 cm rectangles and sonicated in detergent for 30 min, followed by washing in deionized (DI) water, acetone, and ethanol and stored in ethanol. Subsequently, the 10uL as-prepared ink slurry was dropped onto the clean and dry FTO substrate (before using, they were dried by blowing Ar gas) and then we used a blading coating to make the slurry spread evenly on the FTO surface. Finally, they were heated at 90^{o}C for 60 min and then cooled naturally to room temperature.

Characterizations.

Scanning electron microscopy (SEM) images were recorded using a high-resolution scanning electron microscope (EVO MA10, Carl Zeiss, Germany). X-ray diffraction (XRD) spectra were collected at room temperature over a 2θ at a certain range on PANalytical X-ray diffractometer (X'Pert3 Powder) using Cu-Kα radiation of 40 kV. The ultraviolet-visible (UV-VIS) absorption spectra were obtained by using a UV-Vis spectrophotometer (SHIMADZU, UV-2600, Kioto, Japan). The photoluminescence (PL) spectra were recorded by a spectrofluorometer (SHIMADZU, RF-5301PC, Kioto, Japan). Photoluminescence decay was conducted by transient photoluminescence (TRPL) spectrometer (PicoQuant Fluo Time 200). The data was recorded by a time-correlated single-photon counting

(TCSPC) system to explore the PL decay dynamics. The specification of the laser was given as <200 ps pulses with a fluence of ~ 30 nJ/cm2. The PL lifetime, τ_{PL}, was extracted by the software Fluofit (Picoquant). For the temperature-dependent TRPL, a cold circulating system (mrc scientific instrument WBL-100) was connected to the sample holder inside the sample chamber of TRPL with a slow Ar stream introduced during the experiment to avoid any water vapor condensing on the surface of the material.

DFT calculations.

Density functional calculations were carried out with Vienna Ab initio Simulation Package (VASP)[35]. The energy cutoff is 600 eV, which is high enough to converge the energy fluctuations within 1 meV/atom. Global breaking conditions for electronic SC-loop and ionic relaxation loop are defined as 10^{-6} eV and 0.01 eV/Å, respectively. The conjugate gradient algorithm was deployed to relax ions. The partial occupancies are calculated by tetrahedron method with Blöchl corrections. Spin polarization was included for all calculations. A gamma-centered k-point mesh was considered with a grid density of 3×3×1. PAW potentials were employed with PBE functional.

Electrochemistry.

For the cyclic voltammogram (CV) experiment, the three-electrode conventional electrochemical cell consisted of three electrodes, a MBCl-I (or MBI)/FTO as the working electrode, a platinum wire as the counter electrode, and an Ag/Ag^+ electrode as the reference. The measurement was tested under ambient conditions (purged by Ar gas) in CH_2Cl_2 with 0.1M $TBAPF_6$ as the supporting electrolyte. All of these data were obtained on a CH Instruments electrochemical workstation (CHI 760E, Austin, TX)

Photoelectrochemistry.

The PEC measurements were performed on an electrochemical workstation (CHI 760E, Austin, TX). A three-electrode setup, with MBCl-I (MBI)/FTO as the working electrode, a platinum wire as the counter electrode, and an Ag/Ag^+ electrode as the reference, was used to study the photocurrent-voltage (J-V) behaviors. The active area of the working electrode was defined by a 3mm diameter hole. The electrolyte comprises 57 wt % HI aqueous solution saturated with MBCl-I (MBI) powder. The solar light with the power intensity of 100mW cm^{-2} was simulated by a 300 W Xenon lamp mounted with a 430nm filter.

Supporting Information

Supporting Information is available from the Wiley Online Library or from the author.

Acknowledgements

The authors acknowledge financial support from the Research Grants Council of Hong Kong (grant no. CityU 21203518 and F-CityU106/18), Innovation and Technology Commission (grant no. MHP/104/21), Shenzhen Science Technology and Innovation Commission (grant no. JCYJ20210324125612035, R-IND12303 and R-IND12304), City University of Hong Kong (grant no. 7005289, 7005580, 7005720, 9667213, 9667229, 9680331 and 9678291), Australian Research Council (ARC) Discovery Early Career Researcher Award (DE160100589), National Natural Science Foundation of China (61874165, 21833009), as well as Major State Basic Research Development Program of China (2019YFB1503401). Y. Tang and C. H. Mak contributed equally to this work.

Received: ((will be filled in by the editorial staff))
Revised: ((will be filled in by the editorial staff))
Published online: ((will be filled in by the editorial staff))

References

[1] a)N. S. Lewis, D. G. Nocera, *Proceedings of the National Academy of Sciences* **2006**, 103, 15729; b)N. Armaroli, V. Balzani, J.-P. Collin, P. Gaviña, J.-P. Sauvage, B. Ventura, *Journal of the American Chemical Society* **1999**, 121, 4397; c)W. Tu, Y. Xu, J. Wang, B. Zhang, T. Zhou, S. Yin, S. Wu, C. Li, Y. Huang, Y. Zhou, *ACS Sustainable Chemistry & Engineering* **2017**, 5, 7260; d)H.-Y. Hsu, H.-H. Hsieh, H.-Y. Tuan, J.-L. Hwang, *Solar energy materials and solar cells* **2010**, 94, 955; e)J. Zhao, H. Yin, T. Lim, H. Xie, H.-Y. Hsu, F. Forouzan, A. J. Bard, *Journal of The Electrochemical Society* **2016**, 163, D506; f)H. Zhang, Y. Chen, H. Wang, H. Wang, W. Ma, X. Zong, C. Li, *Advanced Energy Materials* **2020**, 10, 2002105; g)L. Yuan, Y.-J. Xu, *Applied Surface Science* **2015**, 342, 154.

[2] a)M. G. Walter, E. L. Warren, J. R. McKone, S. W. Boettcher, Q. Mi, E. A. Santori, N. S. Lewis, *Chemical reviews* **2010**, 110, 6446; b)D. G. Nocera, *Accounts of chemical research* **2017**, 50, 616; c)S. Rao, X. Zou, S. Wang, T. Shi, Y. Lu, L. Ji, H.-Y. Hsu, Q. Xu, X. Lu, *Journal of The Electrochemical Society* **2019**, 166, D427; d)I. Constantinou, T. H. Lai, H. Y. Hsu, S. H. Cheung, E. D. Klump, K. S. Schanze, S. K. So, F. So, *Advanced Electronic Materials* **2015**, 1, 1500167; e)C. Dong, Y. Wang, H. Wang, C. S. K. Lin, H.-Y. Hsu, S.-Y. Leu, *Energy Procedia* **2019**, 158, 918; f)A. J. Bard, M. A. Fox, *Accounts of Chemical Research* **1995**, 28, 141; g)Z. Li, W. Luo, M. Zhang, J. Feng, Z. Zou, *Energy & Environmental Science* **2013**, 6, 347.

[3] W. A. Smith, I. D. Sharp, N. C. Strandwitz, J. Bisquert, *Energy & Environmental Science* **2015**, 8, 2851.

[4] Y. Tang, C. H. Mak, G. Jia, K.-C. Cheng, J.-J. Kai, C.-W. Hsieh, F. Meng, W. Niu, F.-F. Li, H.-H. Shen, X. Zhu, H. M. Chen, H.-Y. Hsu, *Journal of Materials Chemistry A* **2022**, 10, 12296.

[5] S. Park, W. J. Chang, C. W. Lee, S. Park, H.-Y. Ahn, K. T. Nam, *Nature Energy* **2017**, 2, 16185.

[6] Y. Wu, P. Wang, X. Zhu, Q. Zhang, Z. Wang, Y. Liu, G. Zou, Y. Dai, M. H. Whangbo, B. Huang, *Advanced Materials* **2018**, 30, 1704342.

[7] Y. Wu, P. Wang, Z. Guan, J. Liu, Z. Wang, Z. Zheng, S. Jin, Y. Dai, M.-H. Whangbo, B. Huang, *ACS Catalysis* **2018**, 8, 10349.

[8] L. Zhou, Y. F. Xu, B. X. Chen, D. B. Kuang, C. Y. Su, *Small* **2018**, 14, 1703762.

[9] K. M. McCall, C. C. Stoumpos, S. S. Kostina, M. G. Kanatzidis, B. W. Wessels, *Chemistry of Materials* **2017**, 29, 4129.

[10] S. S. Bhosale, A. K. Kharade, E. Jokar, A. Fathi, S.-m. Chang, E. W.-G. Diau, *Journal of the American Chemical Society* **2019**, 141, 20434.

[11] J. Luo, H. Yang, Z. Liu, F. Li, S. Liu, J. Ma, B. Liu, *Materials Today Chemistry* **2019**, 12, 1.

[12] Y. Tang, C. H. Mak, C. Wang, Y. Fu, F.-F. Li, G. Jia, C.-W. Hsieh, H.-H. Shen, J. C. Colmenares, H. Song, M. Yuan, Y. Chen, H.-Y. Hsu, *Small Methods* **2022**, n/a, 2200326.

[13] Y. Tang, C. H. Mak, R. Liu, Z. Wang, L. Ji, H. Song, C. Tan, F. Barrière, H. Y. Hsu, *Advanced Functional Materials* **2020**, 2006919.

[14] K. Eckhardt, V. Bon, J. Getzschmann, J. Grothe, F. M. Wisser, S. Kaskel, *Chemical Communications* **2016**, 52, 3058.

[15] J. Luo, H. Yang, Z. Liu, F. Li, S. Liu, J. Ma, B. Liu, *Materials Today Chemistry* **2019**, 12, 1.

[16] a)Y. Guo, G. Liu, Z. Li, Y. Lou, J. Chen, Y. Zhao, *ACS Sustainable Chemistry & Engineering* **2019**, 7, 15080; b)D. Ju, X. Jiang, H. Xiao, X. Chen, X. Hu, X. Tao, *Journal of Materials Chemistry A* **2018**, 6, 20753.

[17] B. W. Park, B. Philippe, X. Zhang, H. Rensmo, G. Boschloo, E. M. Johansson, *Advanced materials* **2015**, 27, 6806.

[18] a)Y. Zhang, S.-G. Kim, D. Lee, H. Shin, N.-G. Park, *Energy & Environmental Science* **2019**, 12, 308; b)D. Shi, V. Adinolfi, R. Comin, M. Yuan, E. Alarousu, A. Buin, Y. Chen, S. Hoogland, A. Rothenberger, K. Katsiev, *Science* **2015**, 347, 519; c)C. H. Mak, X. Han, M. Du, J.-J. Kai, K. F. Tsang, G. Jia, K.-C. Cheng, H.-H. Shen, H.-Y. Hsu, *Journal of Materials Chemistry A* **2021**, 9, 4454; d)R. Liu, C. H. Mak, X. Han, Y. Tang, G. Jia, K.-C. Cheng, H. Qi, X. Zou, G. Zou, H.-Y. Hsu, *Journal of Materials Chemistry A* **2020**, 8, 23803; e)Y. Yang, Y. Yan, M. Yang, S. Choi, K. Zhu, J. M. Luther, M. C. Beard, *Nature communications* **2015**, 6, 1.

[19] S. D. Stranks, G. E. Eperon, G. Grancini, C. Menelaou, M. J. Alcocer, T. Leijtens, L. M. Herz, A. Petrozza, H. J. Snaith, *Science* **2013**, 342, 341.

[20] a)L. S. Devi, M. K. Al-Suti, C. Dosche, M. S. Khan, R. H. Friend, A. Köhler, *Physical Review B* **2008**, 78, 045210; b)C. H. Mak, X. Huang, R. Liu, Y. Tang, X. Han, L. Ji, X. Zou, G. Zou, H.-Y. Hsu, *Nano Energy* **2020**, 73, 104752; c)Y. Peng, C. H. Mak, J.-J. Kai, M. Du, L. Ji, M. Yuan, X. Zou, H.-H. Shen, S. P. Santoso, J. C. Colmenares, H.-Y. Hsu, *Journal of Materials Chemistry A* **2021**, 9, 26628; d)H.-Y. Hsu, L.

Ji, C. Zhang, C. H. Mak, R. Liu, T. Wang, X. Zou, S.-Y. Leu, E. T. Yu, *Journal of Materials Chemistry C* **2018**, 6, 11552; e)T.-H. Lai, I. Constantinou, C. M. Grand, E. D. Klump, S. Baek, H.-Y. Hsu, S.-W. Tsang, K. S. Schanze, J. R. Reynolds, F. So, *Chemistry of Materials* **2016**, 28, 2433.

[21] a)H.-Y. Hsu, J. H. Vella, J. D. Myers, J. Xue, K. S. Schanze, *The Journal of Physical Chemistry C* **2014**, 118, 24282; b)Z. Chen, H.-Y. Hsu, M. Arca, K. S. Schanze, *The Journal of Physical Chemistry B* **2015**, 119, 7198; c)G. Jia, Y. Pang, J. Ning, U. Banin, B. Ji, *Advanced Materials* **2019**, 31, 1900781.

[22] a)R. A. Marcus, *Reviews of Modern Physics* **1993**, 65, 599; b)C. H. Mak, R. Liu, X. Han, Y. Tang, X. Zou, H. H. Shen, Y. Meng, G. Zou, H. Y. Hsu, *Advanced Optical Materials* **2020**, 8, 2001023.

[23] a)X. Zou, L. Ji, H.-Y. Hsu, K. Zheng, Z. Pang, X. Lu, *Journal of Materials Chemistry A* **2018**, 6, 12724; b)Z. Chen, H.-Y. Hsu, M. Arca, K. S. Schanze, *The Journal of Physical Chemistry B* **2014**, 119, 7198; c)J.-L. Brédas, D. Beljonne, V. Coropceanu, J. Cornil, *Chemical Reviews* **2004**, 104, 4971.

[24] R. A. Marcus, *The Journal of chemical physics* **1956**, 24, 966.

[25] Z. Wang, L. Wang, Y. Xing, D. Yang, J. Yu, Z. Hao, C. Sun, B. Xiong, Y. Han, J. Wang, *ACS Photonics* **2017**, 4, 2078.

[26] a)S. J. Su, E. Gonmori, H. Sasabe, J. Kido, *Advanced Materials* **2008**, 20, 4189; b)W. Li, Y. Pan, L. Yao, H. Liu, S. Zhang, C. Wang, F. Shen, P. Lu, B. Yang, Y. Ma, *Advanced Optical Materials* **2014**, 2, 892; c)S. Wang, J. Yu, M. Zhang, D. Chen, C. Li, R. Chen, G. Jia, A. L. Rogach, X. Yang, *Nano letters* **2019**, 19, 6315; d)X. de Vries, R. Coehoorn, P. A. Bobbert, *Nature communications* **2020**, 11, 1.

[27] S. Jain, S. Verma, S. P. Singh, S. N. Sharma, *Biosensors and Bioelectronics* **2019**, 127, 135.

[28] K. Arora, M. Tomar, V. Gupta, *Biosensors and Bioelectronics* **2011**, 30, 333.

[29] a)E. Laviron, L. Roullier, C. Degrand, *Journal of Electroanalytical Chemistry and Interfacial Electrochemistry* **1980**, 112, 11; b)M. Srivastava, A. K. Das, P. Khanra, M. E. Uddin, N. H. Kim, J. H. Lee, *Journal of Materials Chemistry A* **2013**, 1, 9792; c)H. Muhammad, I. A. Tahiri, M. Muhammad, Z. Masood, M. A. Versiani, O. Khaliq, M. Latif, M. Hanif, *Journal of Electroanalytical Chemistry* **2016**, 775, 157.

[30] a)D. Diamond, *Trends in Analytical Chemistry* **1996**, 1, X; b)J. Wang, *Inc., New York* **2000**, 81.

[31] N. K. Bhatti, M. S. Subhani, A. Y. Khan, R. Qureshi, A. Rahman, *Turkish Journal of Chemistry* **2006**, 29, 659.

[32] N. K. Bhatti, M. S. Subhani, A. Y. Khan, R. Qureshi, A. Rahman, *Turkish Journal of Chemistry* **2006**, 30, 165.

[33] T. N. Murakami, S. Ito, Q. Wang, M. K. Nazeeruddin, T. Bessho, I. Cesar, P. Liska, R. Humphry-Baker, P. Comte, P. Pechy, *Journal of the Electrochemical Society* **2006**, 153, A2255.

[34] H.-Y. Hsu, L. Ji, H. S. Ahn, J. Zhao, E. T. Yu, A. J. Bard, *Journal of the American Chemical Society* **2015**, 137, 14758.

[35] a)G. Kresse, J. Hafner, *Physical review B* **1993**, 47, 558; b)G. Kresse, J. Furthmüller, *Computational Materials Science* **1996**, 6, 15; c)G. Kresse, J. Furthmüller, *Physical Review B* **1996**, 54, 11169; d)G. Kresse, D. Joubert, *Physical Review B* **1999**, 59, 1758.

The table of contents entry should be 50–60 words long and should be written in the present tense. The text should be different from the abstract text.

The interfacial dynamics and electrochemical interactions of hybrid perovskites *prepared by* anion-exchange process in the PEC system was investigated through computational simulation, experimental photophysical and (photo)electrochemical analysis. The synergically interfacial dynamics and electrochemical analysis help to discover the intrinsic and interfacial properties of semiconductor materials.

Y. Tang[a,b,†], C. H. Mak[a,b,†], J. Zhang[c], G. Jia[d], K.-C. Cheng, H. Song[e], M. Yuan[f], S. Zhao[*,c], J.-J. Kai[c], J. C. Colmenares[g], and H.-Y. Hsu[*,a,b]